Engineering Structures 322 (2025) 119115

Contents lists available at ScienceDirect

Engineering Structures

journal homepage: www.elsevier.com/locate/engstruct

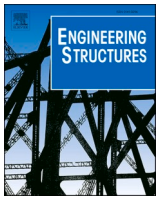

Influence of specimen size and fiber content on fatigue flexural strength of high-performance fiber-reinforced concrete

Álvaro Mena-Alonso *, Miguel A. Vicente, Jesús Mínguez, Dorys C. González

Department of Civil Engineering, University of Burgos, C/ Villadiego s/n, 09001 Burgos, Spain

ARTICLE INFO

Keywords:
Flexural fatigue
Micro-computed tomography
Fiber distribution
Orientation factor
Cyclic creep curve

ABSTRACT

This paper studies the impact of specimen size and fiber content on the flexural fatigue response of high-performance fiber-reinforced concrete (HPFRC). For this purpose, six series of prismatic specimens were fabricated, considering two sizes (75 × 75 × 300 mm and 150 × 150 × 600 mm) and three fiber contents (0.3%, 0.6% and 1%). Twelve specimens from each series were tested in flexural fatigue under the same relative stress levels. It was sought to explain the variations in fatigue response through the observation of the mesostructure. In particular, correlations were established between the fiber distribution and the fatigue strength of all series. The results reveal that the parameter that most influences the ultimate static bending strength (σ_{ult}) is the fiber volume in the central region of the specimens (V_{fib}), with the orientation having a much lower weight. In contrast, the opposite is true for cyclic tests. Since the fatigue stress levels were calculated in relation to σ_{ult} of each series, the influence of V_{fib} is negligible. In this case, a clear correlation between fiber orientation with the longitudinal axis and fatigue strength is observed. Specifically, the orientation factor η_X accurately predicts both the characteristic fatigue life and the rate at which damage progresses in the main macrocrack.

1. Introduction

Fatigue in high-strength fiber-reinforced concrete is a very active field of research at present. This is motivated by the technological advancement of this building material. The new types of ultra high-performance fiber-reinforced concrete (UHPFRC), in addition to having very high compressive strengths (above 120 MPa), have exceptional flexural behavior. Indeed, for high fiber contents of about 2 %, the first-crack strength can even exceed 20 MPa [1,2]. This contributes to the increasing structural responsibility of fiber-reinforced concrete, which is moving from its classic secondary applications to being part of the main resistant elements. On the other hand, thanks to the development of concrete technology, structures are gradually slenderer, which causes cyclic fatigue loads to gain prominence with respect to other actions. In other words, as constructions are lighter, the stabilizing effect of self-weight is less and they are therefore more susceptible to variable actions of a cyclic nature, such as traffic or wind. Two typical examples where fatigue is critical in design are high-speed railroad bridges and concrete wind turbine towers. Consequently, the study of fatigue in concrete is a priority issue in civil engineering.

There are numerous factors that affect the fatigue behavior of high-performance fiber-reinforced concrete (HPFRC), some of which are generic to fatigue in concrete, while others are specific to fiber-reinforced concrete. In the first group lies the element size. It is observed that the fatigue strength in homothetic elements decreases with increasing size [3,4]. This is known as the size effect, and it affects the mechanical behavior of concrete in general. In fact, most of the research on the size effect in fiber-reinforced concrete studies the static flexural strength [5–8], and to a lesser extent the compressive strength [9–11]. In fatigue, publications are scarce, although there has been a growing interest in the last few years [9,11–14]. The recent work of Kumar et al. [14], who tested prismatic UHPFRC specimens of 75, 150 and 300 mm in length under flexural fatigue, is noteworthy. They concluded that, for a load ratio of 0.75, the fatigue life of the small specimens was approximately ten times higher than that of the large ones. This is explained because the fracture process zone, where the crack-bridging strength develops, does not depend on the specimen size, but on intrinsic material parameters; and therefore in small specimens this region is proportionally larger than in large specimens. This conclusion is also stated in other investigations [13,15].

Regarding the particular factors of HPFRC that influence its fatigue response, one of the most relevant is the fiber content. Under static load

* Corresponding author.
E-mail address: amena@ubu.es (Á. Mena-Alonso).

https://doi.org/10.1016/j.engstruct.2024.119115
Received 27 May 2024; Received in revised form 26 September 2024; Accepted 6 October 2024
Available online 12 October 2024

conditions, it is observed that the flexural strength increases linearly with fiber content, at least up to volumes of 5 %, rarely exceeded in practice [16–18]. However, in fatigue this is not true. Several authors point out that fatigue life increases with fiber dosage, but up to a limit [19–21]. Germano et al. [19] performed an experimental study of flexural fatigue in steel fiber-reinforced concrete (SFRC) with 0.5 % and 1 % fibers. The results revealed that for the three load levels considered the fatigue life was higher in the specimens with the lowest fiber content. In compressive fatigue, Poveda et al. [20] determined that the optimum fiber content for which the highest number of cycles was reached in self-compacting SFRC was 0.6 %, with a significant decrease from 0.8 %.

The different fatigue behavior of HPFRC depending on specimen size and fiber content is likely explained by changes in the concrete mesostructure. In other words, different specimen sizes and fiber volumes lead to different configurations of the concrete components (matrix, aggregates, fibers and pores). And some configurations necessarily favor higher fatigue strength than others.

The influence of concrete mesostructure on its mechanical behavior in general, and its fatigue response in particular, is a well-known fact. In plain concrete, some works demonstrate that increases in porosity and pore size reduce fatigue life [22–24]. Others focus on the properties of coarse aggregate, studying the impact of its type and grain size on the number of cycles to failure [25,26]. However, in fiber-reinforced concrete subjected to bending, the component that potentially has the greatest influence on the development of fatigue damage is the fibers. Once the concrete has cracked, the main load-bearing mechanism is the bonding forces generated by the fibers through their adhesion to the matrix [12]. Therefore, the fiber distribution within the specimen significantly determines the magnitude of these forces and consequently the number of cycles it can withstand.

However, publications studying the influence of fiber distribution on the fatigue behavior of concrete are scarce [27–29]. It is worth mentioning the work of González et al. [28], who studied the fiber orientation in SFRC specimens subjected to fatigue by performing wedge-splitting tests. The results revealed a strong correlation between the fatigue damage rate (slope of the secondary section of the cyclic creep curves) and the fiber orientation in around the main crack.

There are different methods to determine the fiber distribution and orientation in a concrete specimen. One of the simplest consists of making a cut in the plane with respect to which the orientation is to be calculated, capturing a high-definition image and, from the ellipsoidal sections of the fibers, calculating their orientation [30]. This technique has many limitations: it is destructive, it only allows to determine the orientation with respect to one plane and has several sources of inaccuracy (flatness of the cutting plane, insufficient resolution for small fibers, etc.). Another more sophisticated technique is the inductive method, which is based on the inductance differences in various directions when generating an electromagnetic field in a concrete specimen [31,32]. The inductive method permits to accurately obtain the fiber volume and average orientations. However, it does not allow determining the exact location and orientation of each individual fiber. Therefore, it is not possible to perform fiber studies in local regions, which is essential to establish correlations with the flexural fatigue response.

In this context, the most robust technique for determining the fiber distribution in concrete is X-ray micro-computed tomography (microCT). This technology is based on the different attenuation that X-rays experience when passing through matter depending on its density. The result of a tomography is a set of grayscale images representing the cross-sections of the sample at each level. In the images, the gray level of each pixel is related to the density at that point, so that lower (darker) gray levels correspond to low densities, and vice versa. The real potential of microCT lies in the post-processing of tomographies using image analysis techniques. Basically, this involves performing a 3D reconstruction of the sample and then segmenting (individually identifying) the components of the mesostructure: pores, fibers, cracks, etc. Segmentation processes are varied, from the simplest ones based on grayscale histogram thresholding to the most complex ones applying convolutional neural networks (CNN) [33,34].

The advantages offered by microCT have turned it into the most widely used technique to study the fiber arrangement in SFRC. There is an extensive literature on works correlating the position and orientation of steel fibers with the macroscopic response of concrete [35–40]. In addition, microCT has also been successfully applied to analyze porosity and cracking patterns [41–44].

This paper arises from the results of [15]. The aim of this work is to study the flexural fatigue behavior of high-performance fiber-reinforced concrete, considering different specimen sizes and fiber volumes. For this purpose, six series of prismatic specimens of two sizes (75 × 75 × 300 mm and 150 × 150 × 600 mm) and with three fiber contents (0.3 %, 0.6 % and 1 %) were fabricated and then subjected to flexural fatigue under the same relative stress levels. It is assumed that different combinations of specimen size and fiber volume result in changes in fiber distribution and orientation, which in turn explain the variations in fatigue response. Therefore, correlations were established between fiber arrangement, obtained through microCT, and fatigue strength.

The paper is structured as follows. Section 2 contains the experimental program, including the description of the materials and specimens, the test procedure and the fiber analysis by microCT. Section 3 presents the results and discussion, analyzing the fiber distribution depending on specimen size and fiber content, as well as establishing correlations between fiber distribution and static and fatigue bending strength. Finally, Section 4 summarizes the conclusions.

2. Experimental program

2.1. Materials and specimens

In this research, steel fiber-reinforced concrete is studied with 3 different fiber contents: 0.3 %, 0.6 % and 1 %. In all three types of concrete, the matrix is identical; that is, the only difference between the three dosages is the fiber volume. In this way, the influence of the fiber content can be evaluated independently, without introducing uncertainties due to other components. In addition, the HPFRC fabricated is self-compacting, thus avoiding heterogeneities due to the vibration process.

Table 1 shows the dosages of the three types of concrete, named A1, A2 and A3 according to the increasing fiber content. To manufacture the concrete, type I Portland cement with a strength class of 52.5 R, produced by Cementos Portland Valderrivas (Pamplona, Spain), was used. The aggregates employed were rolled siliceous gravel from the 4/10 fraction and washed siliceous sand from the 0/4 fraction. To increase the fines content and improve self-compactability, limestone filler I-50, produced by Imeco (Palencia, Spain), was added. Two additives were used: superplasticizer MasterEase 5025 and nanosilica suspension MasterRoc MS 685, both manufactured by Master Builders Solutions (Mannheim, Germany). Finally, the steel fibers used are Dramix RC-80/

Table 1
Concrete dosages.

Component	A1	A2	A3
Cement (kg/m^3)	400.0		
Coarse aggregate (kg/m^3)	538.2		
Fine aggregate (kg/m^3)	847.1		
Filler (kg/m^3)	448.8		
Water (kg/m^3)	160.0		
Superplasticizer (kg/m^3)	16.0		
Nanosilica (kg/m^3)	20.0		
Steel fibers (kg/m^3)	23.6	47.1	78.5
w/c ratio	0.4		
Steel fibers (% vol.)	0.3 %	0.6 %	1.0 %

30-CP, produced by Bekaert (Zwevegem, Belgium). These are hooked-end type fibers with a length of 30 mm and a diameter of 0.38 mm (aspect ratio of 79).

To verify the self-compactability requirements, as well as the resistance to segregation, the three concrete mixtures were subjected to slump flow tests in accordance with EN 12350–8 [45]. Table 2 contains the results of d_f (final diameter of the poured concrete) and t_{50} (time to reach a diameter of 50 cm). In all cases, the limitations for self-compacting concrete set by EFNARC [46] are met. None of the mixes showed signs of segregation or instability.

For each type of concrete, prismatic specimens of two sizes were fabricated: 75 × 75 × 300 mm labeled 'S', and 150 × 150 × 600 mm labeled 'L'. The latter is the standard specimen size for determining the flexural strength in SFRC, according to EN 14651 [47]. The two specimen sizes are homothetic, with a scale factor of 2 in length and 8 in volume. In the central section of all specimens, a notch of h/6 was practiced, where h is the specimen depth. The specimens were notched for the following reasons. First, because this is indicated in EN 14651, the standard followed to characterize the static and flexural fatigue response of the HPFRC. Second, because the notch localizes the fracture plane and allows a more stable cracking than in the case of unnotched beams. The notch leads to a progressive decrease of the effective cross-section at the midspan, and thus of the load-carrying capacity of the beam. For the same geometry, notched beams have a lower bending strength and lower deformation capacity than unnotched beams [48]. In addition, to characterize each type of concrete, cylindrical specimens of 150 × 300 mm were manufactured.

Therefore, in this work, 6 series of prismatic specimens were tested: 3 of size 'S' (A1-S, A2-S and A3-S) and 3 of size 'L' (A1-L, A2-L and A3-L). Fifteen specimens were fabricated per series, making a total of 90. All specimens were stored in a climate chamber at 20 (± 0.1) °C and 95 (± 2) % humidity for one year. The tests began when the concrete was approximately one year and four months old, so it can be assumed that the variation in concrete strength during the experimental campaign is negligible.

Just before the flexural tests, characterization tests of the three types of concrete were carried out. It was concluded that the fiber content hardly affects the compressive strength and modulus of elasticity of the concrete, as also noted by other investigations [49,50]. The mean value of f_c is 106.8 (± 2.1) MPa, while the mean value of E_c is 45.1 (± 1.5) GPa.

2.2. Testing procedure

2.2.1. Monotonic tests

Prior to the fatigue tests, static flexural strength tests were performed in accordance with EN 14651 [47]. The purpose of these tests is to determine the ultimate flexural strength σ_{ult} of all series (i.e., of the three types of HPFRC in the two specimen sizes), since this is the parameter taken as a reference to define the stress levels of the fatigue tests.

In each specimen size, the proportions established in the aforementioned standard [47] were maintained. Thus, in the 'L' specimens the span between supports was 500 mm and the notch depth was 25 mm, while in the 'S' specimens these measurements were 250 and 12.5 mm, respectively. Fig. 1 shows images of a flexural test in the two specimen sizes.

The tests were performed with displacement control, at a speed of 0.08 mm/min until reaching a crack mouth opening displacement (CMOD) of 0.1 mm. Once this value was exceeded, the speed was increased to 0.21 mm/min up to a CMOD of 4 mm, at which point the test was concluded. The load was applied with a dynamic hydraulic actuator 244.21, manufactured by MTS (Eden Prairie, MN, USA), with a load range of ± 50 kN and a displacement amplitude of 150 mm. The parameters recorded were the load, the CMOD and the relative vertical displacement between the supports and the central section. The load was measured with a load cell 661.20F-02, from MTS, incorporated in the actuator. The CMOD was recorded with an axial extensometer 634.12F-24, produced by MTS, with an accuracy of 10 μm and a range of 25 mm. Finally, the displacement was measured with two laser distance meters CP08MHT80, manufactured by Wenglor (Tettnang, Germany), with an accuracy of 8 μm and a range of 50 mm.

Table 2
Results of slump flow test.

Concrete type	d_f (cm)	t_{50} (s)
A1	77	5.1
A2	74	4.9
A3	65	5.5

Table 3 contains the results of ultimate flexural strength σ_{ult} and stress corresponding to the limit of proportionality (LOP) f_L. The former is defined as the maximum stress reached throughout the entire test. The latter is the maximum stress up to a CMOD of 0.05 mm, being an approximation of the first-crack strength. The values in the table are the average of the three tests performed per series.

Table 3 reveals several interesting aspects. First, in all series it is satisfied that $\sigma_{ult} > f_L$, indicating that strain hardening occurs. In other words, the strength of the concrete matrix (pre-cracking) is lower than that of the bonding forces generated by the fibers (post-cracking). This causes that, once cracked, the HPFRC is able to withstand more load. Secondly, the greater the fiber volume, the greater is σ_{ult} and, to a lesser extent, f_L. The increase in ultimate strength is explained by the higher adhesion forces of the fibers. As for the LOP stress, its increase should theoretically be much smaller, since the first-crack strength primarily depends on the concrete matrix rather than the fibers. However, it is likely that from very early stages of cracking (CMOD < 0.05 mm), the fibers start to mobilize, particularly in the series with higher fiber volumes. Finally, a clear size effect is observed, with both σ_{ult} and f_L being greater in the 'S' specimens than in the 'L' ones.

2.2.2. Fatigue tests

The main phase of the experimental campaign involved 3-point bending fatigue tests. These tests consisted of applying cycles of constant amplitude and stress levels until failure. As shown in Table 3, in each series the maximum and minimum stresses of the fatigue cycles were different, since they were calculated as 80 % and 16 % of the ultimate strength σ_{ult} of the corresponding series, respectively. The reason for subjecting all series to the same relative stress levels is to eliminate the influence of variations in static strength. The stress levels of 80 % and 16 % of σ_{ult} (stress ratio of 0.2) were set considering a target fatigue life of 10^4 cycles [19,51–54].

The frequency of the fatigue cycles was 5 Hz. Twelve prisms per series were tested, resulting in a total of 72 fatigue tests. Regarding the geometrical configuration, parameters recorded and sensor setup in the tests, everything mentioned in subsection 2.2.1 applies. Additionally, the fatigue life or number of cycles to failure was monitored.

2.3. Fiber analysis with microCT

To study the fiber distribution within the concrete matrix, the specimens were analyzed using micro-computed tomography. The scans were conducted at the Spanish National Research Center for Human Evolution (CENIEH), located in Burgos (Spain). A microCT system CoreTOM, manufactured by Tescan (Brno, Czech Republic), was used, consisting of a 300 W microfocus tube and a movable flat panel detector. This equipment is capable of reaching resolutions of up to 2 μm and accommodates sample sizes of up to 1 m in height and 45 kg in weight.

All 'S' specimens (A1-S, A2-S and A3-S series) were scanned before the flexural tests. The 15 specimens per series were analyzed, both the 3 static and the 12 fatigue ones. The specimens are scanned in a vertical position, since in this way the cross-section crossed by the conical X-ray beam is minimal, and therefore the quality of the scan is better. To avoid unwanted movements during the scanning process, the specimen is

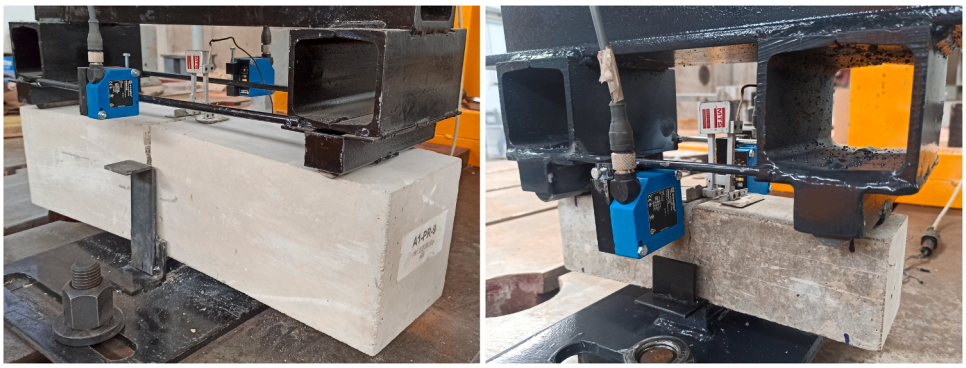

Fig. 1. Flexural strength test on 'L' (left) and 'S' (right) specimens.

Table 3
Mean values of ultimate flexural strength σ_{ult} and LOP stress f_L. Stress levels of fatigue cycles. Ratios between fatigue stress levels and σ_{ult} and f_L, respectively.

Series	Fiber content (%)	σ_{ult} (MPa)	f_L (MPa)	$\sigma_{max,fat}$ (MPa)	$\sigma_{min,fat}$ (MPa)	$\sigma_{max,fat}/\sigma_{ult}$ (%)	$\sigma_{min,fat}/\sigma_{ult}$ (%)	$\sigma_{max,fat}/f_L$ (%)	$\sigma_{min,fat}/f_L$ (%)
A1-S	0.3	8.78	7.36	7.02	1.40	80 %	16 %	95 %	19 %
A1-L		5.93	5.22	4.74	0.95			91 %	18 %
A2-S	0.6	11.78	8.35	9.42	1.88			113 %	23 %
A2-L		11.37	6.67	9.10	1.82			136 %	27 %
A3-S	1	19.65	10.45	15.72	3.14			150 %	30 %
A3-L		16.41	7.74	13.13	2.63			170 %	34 %

placed tightly on an expanded polystyrene base and taped to the base of the device. The preparation of the specimens for CT scanning can be seen in Fig. 2.

As for the 'L' specimens (A1-L, A2-L and A3-L series), it was not possible to scan them prior to testing. The combination of their large cross-sectional area (150×150 mm^2) and the high density of concrete was excessive for the microfocus power, resulting in images of insufficient quality. For this reason, once the tests were finished, 75×75×150 mm mini-prisms obtained from the 'L' specimens were scanned, extracted as close as possible to the notch (Fig. 3). It is assumed that the fiber distribution at the location of the mini-prisms is approximately the same as in the notch region, since they are in close proximity. The mini-prisms were not cut at the midspan section because, after testing, this area was damaged and the position of the fibers was altered. These mini-prisms were cut into a selection of the 'L' specimens: 4 per series, 12 in total.

Fig. 2. Preparation of 'S' size specimens for CT scanning.

As the cross-sectional area of the 'S' specimens and the mini-prisms extracted from the 'L' specimens is the same (75 × 75 mm^2), the scanning parameters were identical, achieving in all cases a resolution of 65 μm. This value is considered sufficient for the correct identification of the fibers.

Once the specimens were scanned, to obtain the individual properties of the fibers in each specimen (position, orientations, etc.), it is necessary to postprocess the microCT images with image analysis techniques. For this purpose, the software Dragonfly, developed by ORS (Montréal, Canada), was used. A specific procedure was implemented in this program to obtain an adequate segmentation of the fibers of each specimen; that is, the separation of the fibers into independent sets of voxels (pixels in 3D).

In some cases, especially in series with a higher fiber volume, conventional segmentation techniques (simple thresholding, watershed segmentation) did not work properly, generating clusters of many fibers that distorted the results. For this reason, the Dragonfly artificial intelligence (AI) tool, which uses convolutional neural networks (CNN), was used. In a simplified form, this interface uses segmentation data manually entered by the user to learn how to transform new CT images into correct segmentation data.

Fig. 4 shows images of the fiber segmentation of three 'S' specimens belonging to the A1-S, A2-S and A3-S series, respectively.

3. Results and discussion

3.1. Fiber distribution depending on specimen size and fiber content

Firstly, the influence of specimen size and fiber content on the fiber arrangement within the concrete matrix is studied. To this end, the data from the post-processing of the microCT images were used.

Since flexural failure in notched specimens is highly localized, it is assumed that the fibers potentially affecting flexural behavior are those located in the central zone of the specimens. Therefore, while in the mini-prisms of the 'L' specimens the whole volume has been considered to analyze the fiber distribution, in the 'S' specimens the study has been restricted to a cubic volume of 75 × 75 × 75 mm^3 centered in the specimen. Therefore, in the 'S' specimens the fibers outside this central zone of 75 mm length have not been taken into account.

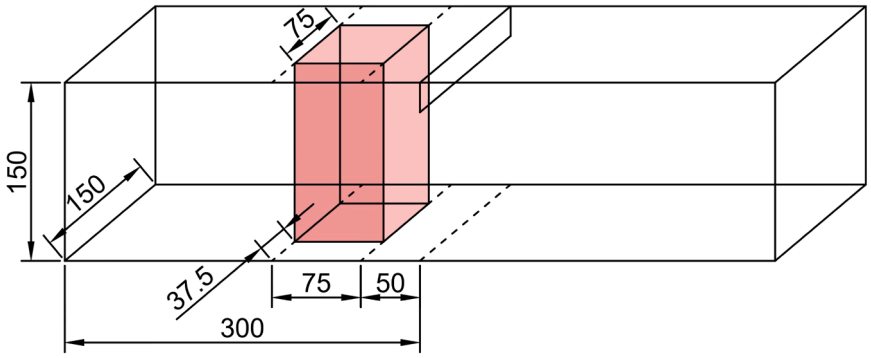

Fig. 3. Identification of mini-prisms obtained from 'L' specimens after 3-point bending fatigue tests.

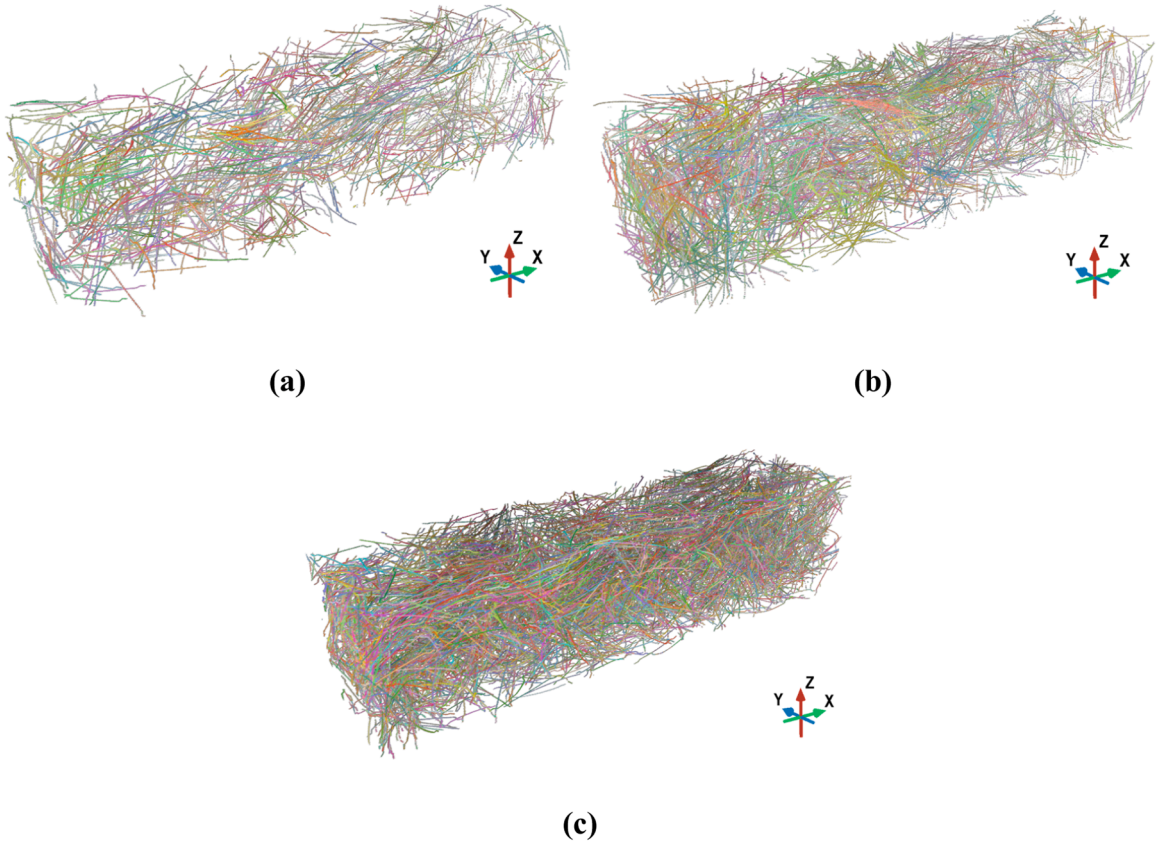

Fig. 4. Fiber segmentation in S-size specimens with different fiber content: (a) A1-S with 0.3 %, (b) A2-S with 0.6 %, (c) A3-S with 1 %.

The two parameters related to fiber distribution to be studied are fiber volume and orientation.

Table 4 contains the results of the relative fiber volume (V_{fib}) and the volume index (vi) for all series. Table 4 contains the results of the relative fiber volume (V_{fib}) and volume index (vi) for all series. The former is defined as the volume of fibers (expressed in %) in the central part of the specimens. That is, in L-size specimens it corresponds to the volume of fibers in the scanned mini-prisms, while in S-size specimens it corresponds to the volume of fibers only in a virtual volume of $75 \times 75 \times 75$ mm^3 centered on them. On the other hand, the volume index is defined as the ratio between V_{fib} and the theoretical fiber volume (0.3 %, 0.6 % or 1 %, depending on the series). These parameters make it possible to measure the level of homogeneity in the distribution of fibers. For example, a value of vi far from 1 indicate that the distribution of fibers in the specimen is heterogeneous. If vi is greater than 1, there are more fibers in the central part than at the ends; if vi is less than 1, the opposite is true. To reach these conclusions, it is considered that the fiber dosage in the complete volume of the specimens coincides with the theoretical one.

Table 4
Mean values of relative fiber volume and volume index.

Series	V_{fib} (%)	vi
A1-S	0.26	0.88
A1-L	0.30	1.00
A2-S	0.65	1.08
A2-L	0.51	0.85
A3-S	1.36	1.36
A3-L	0.78	0.78

A value of V_{fib} and vi is obtained for each specimen. Table 4 includes the average values for each series.

Table 4 shows that the fiber volume in the central region is higher in

the small specimens than in the large ones. In fact, in the series with A2 and A3 concrete types, the fiber volume in the 'S' specimens is above the theoretical value (vi > 1), while in the 'L' specimens the opposite is true. This does not hold true for the A1-S and A1-L series, where the fiber volume in the small specimens is slightly below the theoretical value.

Furthermore, it is observed that the higher the fiber content, the greater the difference in fiber volume between the small and large specimens. Specifically, these differences are −12 %, 27 % and 73 % for the theoretical contents of 0.3 %, 0.6 % and 1 %, respectively. This is clearly illustrated in Fig. 5.

On the other hand, Fig. 6 shows the histograms of fiber orientations with respect to the coordinate axes. The coordinate system is as shown in Fig. 4 and is the same for all series: the X-axis indicates the longitudinal direction, the Y-axis corresponds to the transverse direction and the Z-axis indicates the vertical direction (i.e., the direction of load application).

The first evident conclusion to be drawn from the histograms is that fibers are preferentially aligned with the X-axis; or equivalently, they are perpendicular to the YZ plane. This is explained by the wall effect: fibers are arranged parallel to the mold faces, and therefore tend to align with the longitudinal direction of the specimens. Additionally, it is observed that the alignment with the X-axis is much stronger in the small specimens than in the large ones, which is manifested by more pronounced peaks in the histograms of the 'S' specimens than in those of the 'L' specimens. As pointed out by some authors [11], the thickness of influence of the wall effect (i.e., the depth of the perimeter volume of the specimens where the fiber distribution is affected by the mold walls) is independent of specimen size. Consequently, this phenomenon affects proportionally more small specimens.

Another interesting aspect is that fiber content has much less impact on fiber orientation than specimen size. In the S-size series, the A2-S series has the strongest longitudinal alignment, followed by the A3-S and A1-S series, respectively. However, the differences are not very significant. Regarding the L-size series, the most notable observation is that the A1-L series behaves differently from the other two. In particular, the fibers of this series are worse aligned with the X-axis; in fact, their longitudinal orientation is markedly random. In addition, the fibers are more perpendicular to the vertical Z-axis and less to the transverse Y-axis.

Although the histograms provide much information, it is sometimes useful to use parameters to characterize fiber orientation in a simplified way. Table 5 contains the values of the average angle and orientation factor of the 6 series with respect to the 3 coordinate axes. The orientation factor, also called orientation efficiency index, is defined as the average projection of the unit vectors of the fibers in a certain direction. Therefore, it is calculated according to the expression Eq. (1) [55,56]:

$$\eta_\theta = \frac{1}{N_f}\sum_{i=1}^{N_f} \cos\alpha_\theta^i \tag{1}$$

where N_f is the total number of fibers in the volume of concrete considered, α_θ^i is the angle between the i-th fiber and the θ-axis, and finally θ is the corresponding coordinate axis X, Y or Z. Therefore, η_θ takes values between 0 and 1, where 1 indicates that all fibers are parallel to the θ axis, and 0 that they are all perpendicular. The values in the table correspond to the average values of all the scanned specimens in each series.

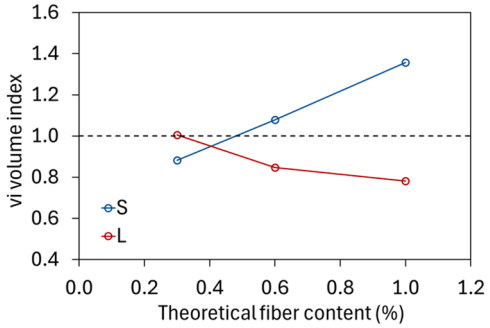

Fig. 5. Theoretical fiber content vs. volume index.

Table 5 confirms the conclusions drawn from the histograms. It is observed that in all series η_X is clearly higher than η_Y and η_Z, indicating that the fibers are longitudinally aligned. Furthermore, while in the 'S' specimens η_X ranges between 0.74 and 0.79, in the 'L' specimens it varies between 0.62 and 0.67. Therefore, it can be stated that the fibers are better aligned with the longitudinal axis in the small specimens, regardless of the content. Finally, it can be seen that, within each specimen size, the series with the lowest fiber content (A1-S and A1-L) are the ones that present the lowest orientation factor in X, remaining practically constant for the series with contents of 0.6 % and 1 %. This indicates that an increase in fiber dosage improves the longitudinal orientation of the fibers, possibly due to the interaction between them within the cement paste. However, the results suggest that this effect would stabilize from a fiber content of around 0.6 %. This can be explained because the increase in fiber volume also causes a reduction in flowability, mitigating the wall effect and thus making it difficult for the fibers to align parallel to the major direction of the mold [38].

3.2. Correlation between fiber distribution and static flexural strength

As mentioned in subsection 2.2.1, strain hardening is observed in the static flexural response of all series. This means that the resistant mechanism of the fibers (post-cracking), rather than that of the concrete matrix (pre-cracking), determines the flexural strength of the HPFRC. The magnitude of the bonding forces originated by the fibers to withstand the bending stresses mainly depends on their arrangement within the concrete. Therefore, it is expected a good correlation between some parameters of the fiber distribution and the ultimate flexural strength. Fig. 7a represents the linear regression between σ_{ult} and the relative fiber volume V_{fib}, considering the mean values of each series.

Fig. 7a reveals a very good correlation between the relative fiber volume and the ultimate flexural strength, such that the higher V_{fib}, the higher σ_{ult}. On the one hand, it is observed that the parameter V_{fib} explains the increase in ultimate strength with increasing theoretical fiber content, which is expected. On the other hand, and more remarkably, V_{fib} also explains the increase in ultimate strength with decreasing specimen size. That is, the fact that σ_{ult} is higher in small specimens than in large ones is largely due to the higher fiber volume V_{fib} in the central region of the 'S' specimens compared to the 'L' specimens, despite having the same theoretical content. This may be because fibers are not homogeneously distributed along the entire length of the specimen, tending to concentrate more at the ends in the large specimens, and more in the center in the small ones. Moreover, it seems that this phenomenon is stronger the higher the fiber content: while the values of V_{fib} in the A1-S and A1-L series are very similar and practically equal to the theoretical content, in the A3-S and A3-L series they are very different, being much higher in the small specimens than in the large ones.

Fig. 7b depicts the linear regression between the relative fiber volume and the stress at the limit of proportionality. It is observed that, despite a good linear correlation between both parameters, V_{fib} is a better predictor variable of σ_{ult} than of f_L (R^2 coefficients of 0.89 and 0.77, respectively). This makes sense, since the stress at the LOP depends, not only on the bonding forces of the fibers, but also on the strength of the concrete matrix itself.

Another parameter related to fiber distribution that can affect the static response in bending is the orientation; in particular, the orientation relative to the longitudinal axis, since it is the axis orthogonal to the theoretical plane of failure. Fig. 8 represents the orientation factor on the X-axis with respect to the ultimate flexural strength, considering the mean values of each series.

Fig. 8 reveals that overall there is a weak relationship between η_X and

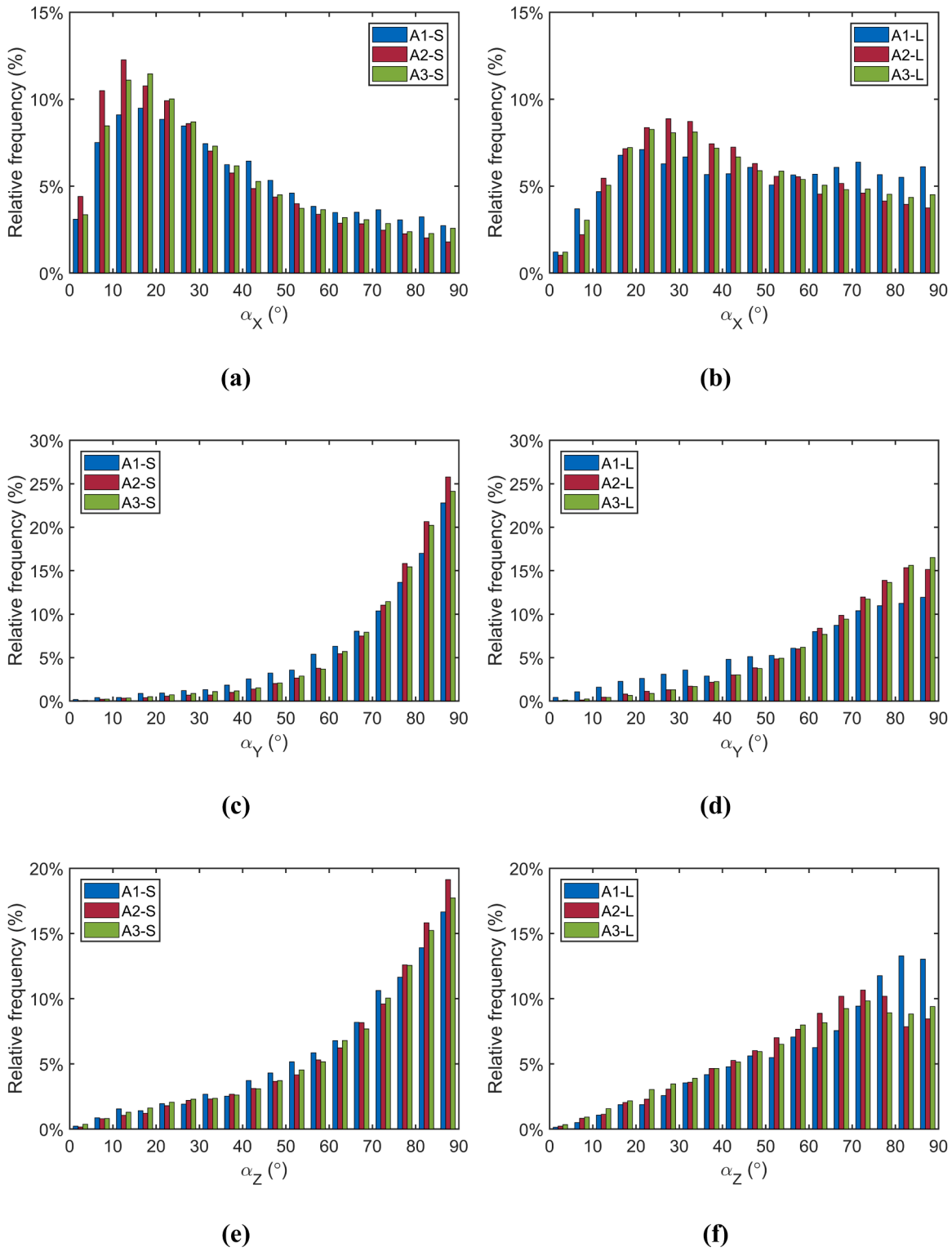

Fig. 6. Histograms of fiber orientation of all series with respect to the coordinate axes: (a,b) X-axis, (c,d) Y-axis, (e,f) Z-axis.

σ_{ult}. On the one hand, the orientation factor on the X-axis does not explain the increase in ultimate strength with increasing fiber content. In other words, there is no clear trend showing that orientation improves with fiber content, and that explains the increase in flexural strength. However, on the other hand, η_X does partially explain the increase in σ_{ult} with decreasing specimen size. It can be seen that the S-size series, which have a higher flexural strength, exhibit a higher orientation factor.

In conclusion, it can be stated that the parameter of fiber distribution that has the greatest influence on flexural strength is the fiber volume in the central region. The variations in V_{fib} explain reasonably well the variations in σ_{ult} across series with different specimen sizes and theoretical fiber contents. Conversely, the role of orientation is secondary since the orientation factor would only partly explain the increase in strength with decreasing specimen size.

Table 5
Mean values of fiber angles and orientation factors with respect to the coordinate axes.

Series	X-axis (longitudinal)		Y-axis (transversal)		Z-axis (vertical)	
	$\alpha_{m,X}$ (°)	η_X	$\alpha_{m,Y}$ (°)	η_Y	$\alpha_{m,Z}$ (°)	η_Z
A1-S	37.0	0.74	71.0	0.31	65.6	0.38
A1-L	47.5	0.62	61.8	0.44	63.3	0.42
A2-S	32.0	0.79	74.6	0.25	67.5	0.35
A2-L	43.6	0.67	68.6	0.35	60.0	0.47
A3-S	34.0	0.77	73.7	0.27	66.4	0.37
A3-L	44.3	0.66	69.0	0.34	59.2	0.47

3.3. Fatigue response

In this subsection, the results of the flexural fatigue tests are presented. Table 6 contains the number of loading cycles until failure in the 12 specimens of each series. It is worth mentioning that in some tests of the A1-S, A1-L and A2-S series, an initial fatigue phase was identified in which concrete was not cracked, i.e., a main macrocrack had not yet been formed from the notch. This phase is characterized by small CMODs (< 0.05 mm), with a highly variable extent in terms of number of cycles between tests. It was assumed that during this period the damage to the concrete is very low and the loads are supported by the matrix, with minimal intervention of the fibers. Therefore, since this study aims to correlate fiber distribution with fatigue behavior, the cycles associated with this phase were excluded.

Note that the reason that in the A1-S, A1-L and A2-S series an initial fatigue phase in the uncracked regime is observed is that in these series the maximum fatigue stress $\sigma_{max,fat}$ is lower than the first crack stress f_L. That is, the ratio $\sigma_{max,fat}/f_L$ is lower or slightly higher than 100 %, as shown in Table 3. Therefore, in these series at the beginning of the tests the concrete is not cracked and the fibers have hardly been mobilized.

During the testing campaign, two incidences occurred. A specimen of the A2-S series showed anomalous behavior, reaching the runout limit set at 10^6 cycles without cracking. Additionally, a specimen of the A2-L series was lost due to a failure in the test control.

Table 6 reveals that all series present a large dispersion in fatigue life, even exceeding two orders of magnitude. At first glance interpreting the results is challenging, thus it is advisable to fit them to the two-parameter Weibull distribution function. This probability model fits well to the statistical distribution of N in concrete fatigue, as pointed out by numerous papers [20,52]. The cumulative Weibull distribution function is expressed as in Eq. (2):

$$F(x) = 1 - \exp\left\{-(x/\lambda)^{\beta}\right\} \quad (2)$$

where x is log N, λ is the scale parameter and β is the shape parameter. The first is related to the characteristic fatigue life, such that the higher λ, the higher the fatigue life. The second is related to the dispersion, so the larger β, the lower the variability of the data.

In Fig. 9 the Weibull fits to the N results of the 6 series are plotted. Table 7 contains the values of the fitting parameters as well as the fatigue life for a cumulative probability of 0.5.

Interesting conclusions can be drawn from Fig. 9 and Table 7. First, in all types of HPFRC, the small specimens withstand more cycles than the large ones, regardless of the fiber content. This size effect in N is particularly noticeable in the series with 0.6 % fibers, being less pronounced in the others. In fact, in the A3-S and A3-L series the fitting curves are nearly identical. Secondly, there is no clear trend in the impact of fiber content on fatigue life; that is, an increase in fiber volume

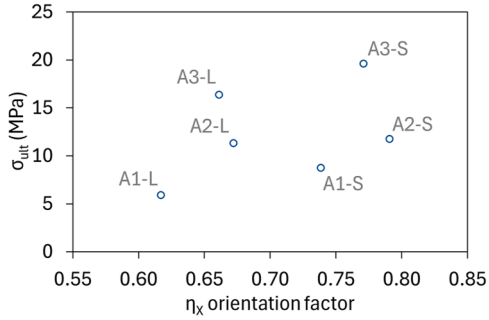

Fig. 8. X-axis orientation factor vs. ultimate flexural strength.

Table 6
Fatigue life (N).

Test No.	0.3 % fibers		0.6 % fibers		1 % fibers	
	A1-S	A1-L	A2-S	A2-L	A3-S	A3-L
1	5775	2325	3463	25,926	18,889	15
2	2914	703	9812	37	918	23,308
3	3665	1570	40,808	-	30	13
4	43	17	19,344	3476	3176	3335
5	694	21,892	22,428	2004	12,888	15
6	2742	1117	0 *	6597	7195	5747
7	7108	52	26,252	32	15,225	9604
8	3629	126	20,746	8851	12	3498
9	1495	4	5156	46	31	5634
10	4329	13	5068	84	3090	102
11	1710	18,876	14,233	2415	3743	1618
12	48	42,491	5024	4264	2219	12,964

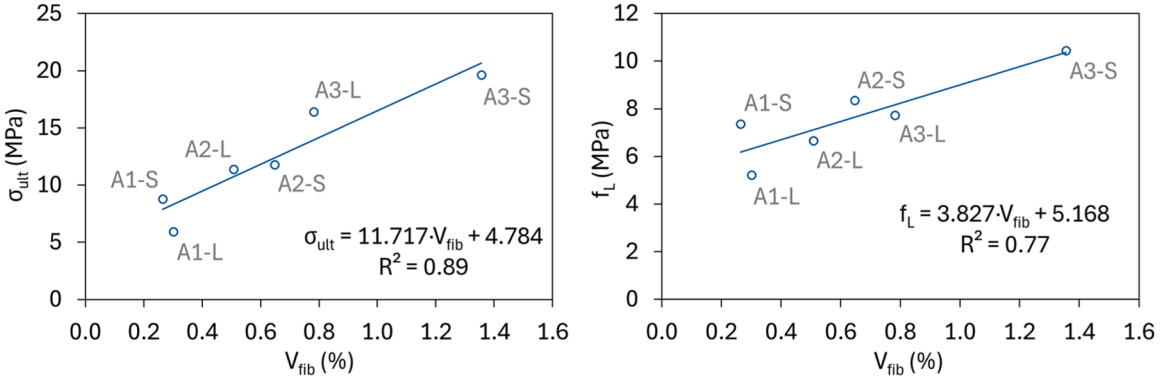

(a) **(b)**

Fig. 7. Linear regression of relative fiber volume with ultimate flexural strength (a) and LOP stress (b).

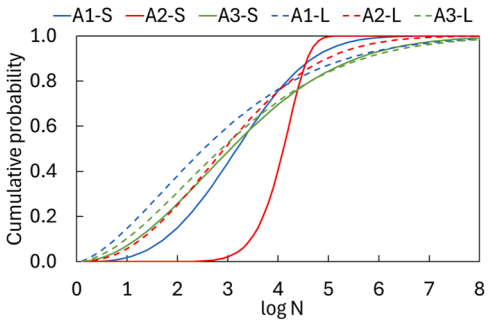

Fig. 9. Weibull fit of fatigue life.

Table 7
Weibull fitting parameters and N for a cumulative probability of 0.5.

Series	λ	6	$N_{p=0.5}$
A1-S	3.58	3.11	1528
A1-L	3.18	1.59	334
A2-S	4.25	10.97	12,764
A2-L	3.44	2.28	851
A3-S	3.67	2.01	1135
A3-L	3.54	1.76	750

does not necessarily lead to an increase in N. Finally, the A2-S series exhibits a different statistical behavior from the rest of the series, with a much higher fatigue life and very low dispersion. As shown in Table 6, this series is the only one in which all specimens exceed 10^3 cycles.

On the other hand, although the number of cycles indicates the moment when fatigue failure occurs, it does not provide any information on the evolution of the internal damage that necessarily occurs in the concrete. Therefore, it is useful to have additional tools to characterize the crack development due to cyclic loading. One of the most interesting ones are the cyclic creep curves, which represent the maximum CMOD at each cycle versus the number of cycles.

Cyclic creep curves in HPFRC typically have the shape shown in Fig. 10. Three stages can be distinguished. Stage (I) corresponds to the initiation of a macrocrack at the notch edge, with subsequent loading of the fibers in that region. Stage (II) represents the stable progression of the macrocrack due to the progressive failure of the fibers. Finally, stage (III) corresponds to the unstable propagation of the macrocrack because of insufficient fiber strength, culminating in global failure.

From the cyclic creep curves, the secondary crack opening rate (dCMOD/dn) can be obtained, defined as the slope of stage (II), which being approximately linear can be fitted to a straight line. This parameter represents the growth rate of the macrocrack; that is, the rate at which fatigue damage is inflicted. Some works indicate that there is a good correlation between the logarithms of dCMOD/dn and N [19,52].

Table 8 contains the values of the secondary crack opening rate in all fatigue tests.

Finally, Fig. 11 shows images of the fatigue failure macro-cracking in a representative test of each series. It is clearly seen that, as the fiber dosage increases, so does the deformation capacity of the specimens. It is observed that damage is more dispersed in specimens with more fibers, while failure is more local and concentrated in specimens with fewer fibers. With respect to the effect of element size, it is concluded that, at equal fiber dosage, the behavior is more ductile in the small specimens; in other words, the ratio representing the size of the fracture zone with respect to the element size is higher in the small specimens. As for the failure modes of the fibers, it is observed that pull-out is the most common, i.e., failure due to loss of adhesion between the fiber and the matrix. Tensile failures are proportionally much smaller.

3.4. Correlation between fiber distribution and flexural fatigue behavior

In subsection 2.2 it is demonstrated that the static flexural strength is conditioned by the relative fiber volume in the central region, such that the higher V_{fib}, the higher σ_{ult}. However, in the case of fatigue tests, a good correlation between V_{fib} and fatigue life is not expected. This is because the cyclic stress levels $\sigma_{max,fat}$ and $\sigma_{min,fat}$ for each series were calculated based on the ultimate flexural strength σ_{ult}. Consequently, the effect of the variations of V_{fib} on the fatigue response is mitigated.

In contrast, it is possible that other parameters related to fiber distribution can explain the different fatigue behavior depending on fiber content and specimen size. Fig. 12 shows the linear regression between the Weibull parameter λ of each series, representative of the characteristic fatigue life, and the average X-axis orientation factor, indicative of the fiber arrangement with respect to the failure plane.

Fig. 12 reveals a good correlation between η_X and λ, reaching an R^2 value of 0.73. Therefore, it is concluded that the X-axis orientation factor is a reliable parameter to predict the fatigue life of HPFRC, considering different fiber contents and specimen sizes. It is evidenced that, in each type of concrete, small specimens have more efficient fiber orientation, leading to higher fatigue strength. On the other hand, the value of η_X also explains how the fatigue response changes depending on the quantity of fibers. It is observed that the A1-S and A1-L series, which endured the lowest number of cycles at each specimen size, are precisely those with the lowest orientation factor. In addition, the A2-S series, which has the highest fatigue life of all, exhibits the highest value of η_X.

On the other hand, Fig. 13 shows the linear correlation between the secondary crack opening rate and the X-axis orientation factor. The values represented are the average of each series.

Some interesting results are obtained from Fig. 13. First, the correlation between η_X and dCMOD/dn is very strong, with coefficients of determination R^2 exceeding 0.90. It is observed that a fiber orientation more perpendicular to the failure plane (higher η_X) results in slower fatigue damage progression (lower dCMOD/dn). Second, the relationship between the two parameters depends on the specimen size. The regression lines, which are nearly parallel, have an offset in the

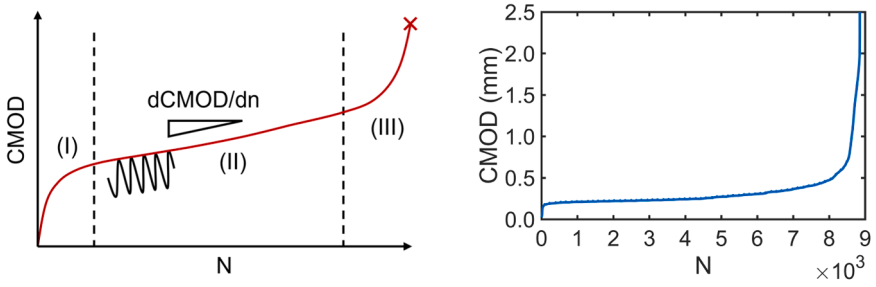

(a) **(b)**

Fig. 10. Cyclic creep curves: (a) theoretical sketch, (b) real curve in specimen no. 9 of series A2-L.

Table 8
Secondary crack opening rate (dCMOD/dn). Units in mm/cycle.

Test No.	0.3 % fibers		0.6 % fibers		1 % fibers	
	A1-S	A1-L	A2-S	A2-L	A3-S	A3-L
1	1.63E−05	2.26E−04	3.11E−05	1.05E−05	6.55E−06	1.04E−01
2	8.58E−05	2.59E−03	1.58E−05	8.11E−02	1.02E−04	1.55E−05
3	4.18E−05	8.03E−04	3.65E−06	-	4.17E−02	1.02E−01
4	4.19E−02	6.88E−02	6.95E−06	7.28E−05	3.14E−05	1.31E−04
5	4.46E−04	4.30E−06	7.62E−06	1.15E−04	3.26E−06	1.05E−01
6	7.43E−05	1.27E−03	-	2.98E−05	3.74E−06	2.92E−05
7	3.00E−05	2.28E−02	3.55E−06	5.73E−02	2.78E−06	8.69E−06
8	2.06E−04	1.44E−02	3.48E−06	2.25E−05	1.72E−01	6.54E−05
9	4.64E−04	3.26E−01	2.16E−05	3.82E−02	5.78E−02	2.99E−05
10	1.30E−04	1.59E−01	3.87E−05	3.16E−02	1.78E−05	1.64E−02
11	3.20E−04	9.08E−06	1.90E−05	1.48E−04	1.97E−05	3.61E−04
12	4.28E−01	4.14E−06	3.18E−05	6.66E−05	6.49E−06	1.19E−05

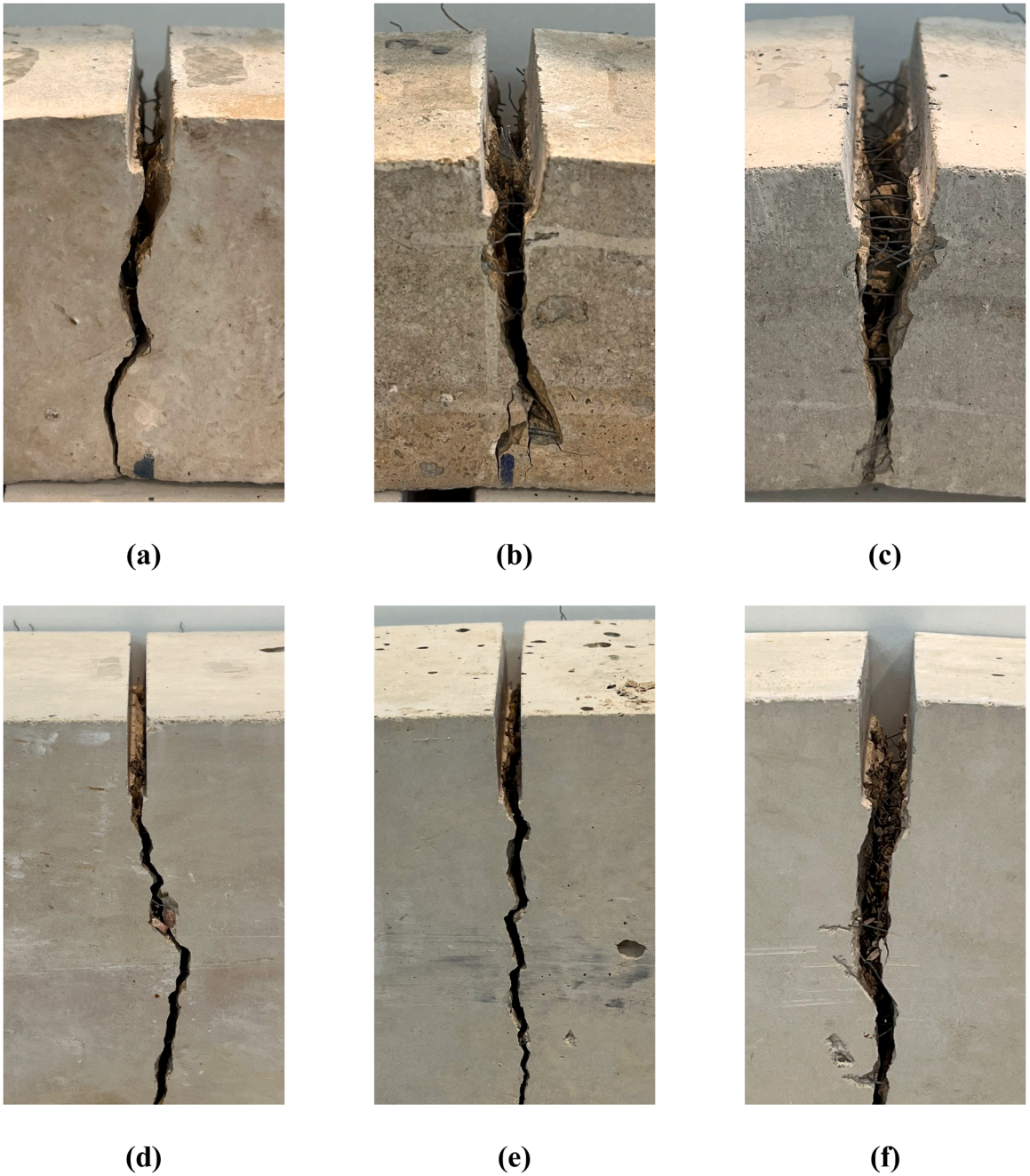

Fig. 11. Images of flexural fatigue failure sections in a representative test of each series: (a) A1-S, (b) A2-S, (c) A3-S, (d) A1-L, (e) A2-L and (f) A3-L.

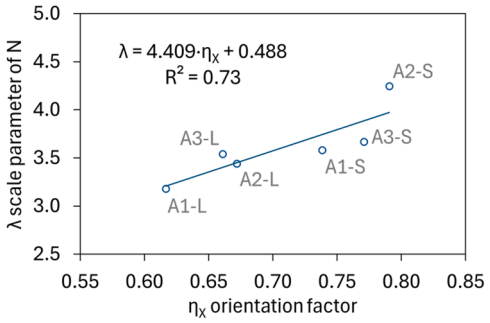

Fig. 12. Linear regression of X-axis orientation factor with Weibull λ parameter.

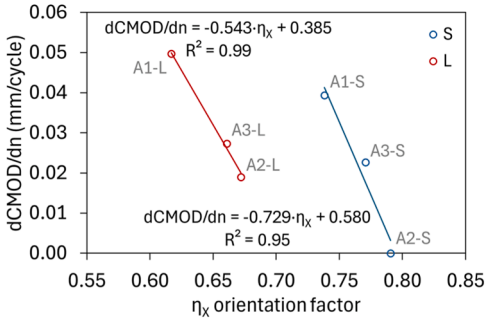

Fig. 13. Linear regression of X-axis orientation factor with secondary crack opening rate.

horizontal direction. Consequently, there is a scaling factor; that is, the value of fiber orientation (η_X) that induces a certain fatigue damage rate (dCMOD/dn) varies depending on the element size. It can be seen that, in both 'S' and 'L' specimens, the series with 0.6 % fibers have the best fiber orientation and the lowest fatigue damage rate, followed by those with 1 % and finally 0.3 % contents.

Comparing with Fig. 12, it can be stated that the orientation factor η_X predicts more accurately the secondary crack opening rate than the fatigue life. This can be explained as follows. The parameter dCMOD/dn represents the average rate at which fatigue cracking grows in the specimen, since it is associated with stage (II) of the cyclic creep curves, the most extensive and which most determines the fatigue response (Fig. 10). On the other hand, the orientation factor η_X indicates the average orientation of the fibers in the central region of the specimen. Since fatigue damage develops in this area, a relationship between dCMOD/dn and η_X is expected. In contrast, the fatigue life indicates the moment at which the cross-section fails because the external loads are greater than the bonding forces of the fibers. Therefore, the fibers that most influence the ultimate failure of the element are mainly those that are mobilized at the end of the fatigue life, rather than those that have been failing (closer to the notch edge). Since η_X represents the orientation of all the fibers in the central region, and not only those in the failure zone, its correlation with N is worse.

In any case, Figs. 12 and 13 demonstrate that fiber orientation explains the differences in the fatigue behavior of HPFRC with different specimen sizes and fiber contents. In particular, the orientation factor with respect to the X-axis (normal to the crack plane) shows a strong correlation with the characteristic fatigue life, as well as with the rate at which the main macrocrack grows.

4. Conclusions

In this work, the flexural fatigue behavior of HPFRC with different element sizes and fiber contents is studied. It is assumed that the variations in fatigue strength observed are caused by variations in the concrete mesostructure; specifically, in the fibers, which largely govern the fracture behavior. Therefore, the aim is to establish solid correlations between fiber distribution and fatigue life.

The most relevant conclusions of this paper are summarized below:

- The analysis of fiber distribution through microCT reveals that the fiber volume in the central region of the specimens clearly differs from the theoretical value, being higher in the small specimens than in the large ones. Moreover, as the theoretical fiber content increases, the difference in real volume between the two specimen sizes increases.
- Regarding the orientation, it is observed that in the small specimens the fibers are better aligned with the X-axis (longitudinal). In contrast, the influence of the theoretical fiber content is lower. In both sizes the highest orientation factor η_X is obtained for 0.6 % of fibers, although the differences are small.
- There is a clear correlation between the fiber volume in the central region of the specimens and the ultimate static flexural strength. The parameter V_{fib} explains by itself the variations of σ_{ult} due not only to the different theoretical fiber contents, but also to the different specimen sizes.
- With respect to fatigue behavior, the influence of V_{fib} is negligible since each series was tested under the same relative stress levels with respect to σ_{ult}. In this case, the parameter that most influences fatigue life for the different fiber contents and specimen sizes is the orientation factor in the longitudinal direction. The correlation of η_X with the Weibull parameter λ, indicative of the characteristic fatigue life, is robust, with an R^2 value of 0.73.
- Additionally, the X-axis orientation factor accurately predicts the secondary crack opening rate, which represents the rate at which fatigue damage progresses in the main macrocrack. In fact, the level of correlation of η_X with dCMOD/dn is higher than with λ. However, it is noted that this relationship depends on the specimen size.

It can be concluded that the results of this research have potential implications in the fatigue design of fiber-reinforced concrete. An adequate knowledge of fiber distribution, using techniques such as micro-computed tomography or the inductive method, can help to estimate more accurately the fatigue life, considering elements of different sizes and with different fiber contents.

CRediT authorship contribution statement

Álvaro Mena-Alonso: Writing – review & editing, Writing – original draft, Methodology, Investigation, Formal analysis. **Miguel A. Vicente:** Writing – review & editing, Supervision, Resources, Funding acquisition, Conceptualization. **Jesús Mínguez:** Writing – review & editing, Resources, Methodology. **Dorys C. González:** Writing – review & editing, Resources, Methodology, Investigation, Funding acquisition.

Declaration of Competing Interest

The authors declare that they have no known competing financial interests or personal relationships that could have appeared to influence the work reported in this paper.

Acknowledgments

The authors are grateful for the financial support of the Spanish Ministerio de Economía y Competitividad (grant no. PID2019–110928RB-C32) and the Spanish Ministerio de Ciencia, Innovación y Universidades (grant no. FPU19/02685).

Data Availability

The raw/processed data required to reproduce these findings cannot be shared at this time as the data also forms part of an ongoing study.

References

[1] Lee SI, Kim JH, Han SJ, Jeong H, Seo SY, Su Kim K. Tension-softening behavior of UHPFRC based on fracture energy. Structures 2022;38:361–74. https://doi.org/10.1016/j.istruc.2022.01.086.

[2] Chu SH, Wang JQ, Kwan AKH. Flexural strength and toughness of self-leveling UHPFRC. Compos Struct 2023;315. https://doi.org/10.1016/j.compstruct.2023.116921.

[3] Le JL, Bažant ZP. Unified nano-mechanics based probabilistic theory of quasibrittle and brittle structures: II. Fatigue crack growth, lifetime and scaling. J Mech Phys Solids 2011;59:1322–37. https://doi.org/10.1016/j.jmps.2011.03.007.

[4] Bažant ZP, Xu K. Size effect in fatigue fracture of concrete. Acids Mater J 1991;88:390–9.

[5] Bažant ZP, Planas J. Fracture and size effect in concrete and other quasibrittle materials. Fracture and Size Effect in Concrete and Other Quasibrittle Materials. Taylor & Francis,; 1998. https://doi.org/10.1201/9780203756799.

[6] Ghasemi M, Ghasemi MR, Mousavi SR. Studying the fracture parameters and size effect of steel fiber-reinforced self-compacting concrete. Constr Build Mater 2019;201:447–60. https://doi.org/10.1016/j.conbuildmat.2018.12.172.

[7] Yoo DY, Banthia N, Yang JM, Yoon YS. Size effect in normal- and high-strength amorphous metallic and steel fiber reinforced concrete beams. Constr Build Mater 2016;121:676–85. https://doi.org/10.1016/j.conbuildmat.2016.06.040.

[8] Nguyen DL, Kim DJ, Ryu GS, Koh KT. Size effect on flexural behavior of ultra-high-performance hybrid fiber-reinforced concrete. Compos B Eng 2013;45:1104–16. https://doi.org/10.1016/j.compositesb.2012.07.012.

[9] Ortega JJ, Ruiz G, Poveda E, González DC, Tarifa M, Zhang XX, et al. Size effect on the compressive fatigue of fibre-reinforced concrete. Constr Build Mater 2022;322:126238. https://doi.org/10.1016/j.conbuildmat.2021.126238.

[10] Fládr J, Bílý P. Specimen size effect on compressive and flexural strength of high-strength fibre-reinforced concrete containing coarse aggregate. Compos B Eng 2018;138:77–86. https://doi.org/10.1016/j.compositesb.2017.11.032.

[11] González DC, Mena Á, Ruiz G, Ortega JJ, Poveda E, Mínguez J, et al. Size effect of steel fiber–reinforced concrete cylinders under compressive fatigue loading: Influence of the mesostructure. Int J Fatigue 2022. https://doi.org/10.1016/j.ijfatigue.2022.107353.

[12] Zhang J, Stang H, Li VC. Fatigue life prediction of fiber reinforced concrete under flexural load. Int J Fatigue 1999;21:1033–49. https://doi.org/10.1016/S0142-1123(99)00093-6.

[13] Mena-Alonso Á, González DC, Mínguez J, Vicente MA. Size effect on the flexural fatigue behavior of high-strength plain and fiber-reinforced concrete. Constr Build Mater 2024;411:134424. https://doi.org/10.1016/j.conbuildmat.2023.134424.

[14] Kumar B, Sharma A, Ray S. Characterization of crack-bridging and size effect on ultra-high performance fibre reinforced concrete under fatigue loading. Int J Fatigue 2024;182. https://doi.org/10.1016/j.ijfatigue.2024.108158.

[15] Á. Mena-Alonso, Flexural fatigue of high-strength plain and fiber-reinforced concrete: influence of mesostructure and study of size effect [PhD Thesis], University of Burgos, 2023. https://doi.org/10.36443/10259/7855.

[16] Vuong TNH, Nguyen TK, Nguyen DL, LE HV, Tran NT. Fiber fraction-dependent flexural behavior of high-performance fiber-reinforced concrete under static and repeated loading. J Build Eng 2023;79. https://doi.org/10.1016/j.jobe.2023.107808.

[17] Yoo DY, Shin HO, Yang JM, Yoon YS. Material and bond properties of ultra high performance fiber reinforced concrete with micro steel fibers. Compos B Eng 2014;58:122–33. https://doi.org/10.1016/j.compositesb.2013.10.081.

[18] Kang ST, Lee Y, Park YD, Kim JK. Tensile fracture properties of an Ultra High Performance Fiber Reinforced Concrete (UHPFRC) with steel fiber. Compos Struct 2010;92:61–71. https://doi.org/10.1016/j.compstruct.2009.06.012.

[19] Germano F, Tiberti G, Plizzari G. Post-peak fatigue performance of steel fiber reinforced concrete under flexure. Mater Struct 2016;49:4229–45. https://doi.org/10.1617/s11527-015-0783-3.

[20] Poveda E, Ruiz G, Cifuentes H, Yu RC, Zhang X. Influence of the fiber content on the compressive low-cycle fatigue behavior of self-compacting SFRC. Int J Fatigue 2017;101:9–17. https://doi.org/10.1016/j.ijfatigue.2017.04.005.

[21] Gao D, Gu Z, Tang J, Zhang C. Fatigue performance and stress range modeling of SFRC beams with high-strength steel bars. Eng Struct 2020;216. https://doi.org/10.1016/j.engstruct.2020.110706.

[22] Chandrappa AK, Biligiri KP. Effect of pore structure on fatigue of pervious concrete. Road Mater Pavement Des 2019;20:1525–47. https://doi.org/10.1080/14680629.2018.1464500.

[23] Oneschkow N, Timmermann T. Influence of the composition of high-strength concrete and mortar on the compressive fatigue behaviour. Mater Struct/Mater Et Constr 2022;55. https://doi.org/10.1617/s11527-021-01868-7.

[24] Vicente MA, González DC, Mínguez J, Tarifa MA, Ruiz G, Hindi R. Influence of the pore morphology of high strength concrete on its fatigue life. Int J Fatigue 2018;112:106–16. https://doi.org/10.1016/j.ijfatigue.2018.03.006.

[25] Peng Q, Wang L, Lu Q. Influence of recycled coarse aggregate replacement percentage on fatigue performance of recycled aggregate concrete. Constr Build Mater 2018;169:347–53. https://doi.org/10.1016/j.conbuildmat.2018.02.196.

[26] Kasu SR, Deb S, Mitra N, Muppireddy AR, Kusam SR. Influence of aggregate size on flexural fatigue response of concrete. Constr Build Mater 2019;229. https://doi.org/10.1016/j.conbuildmat.2019.116922.

[27] Zhan J, Nussbaumer A, Brühwiler E. Influence of fiber orientation on the high cycle tensile fatigue resistance of Ultra-High Performance Fiber Reinforced Cementitious Composites (UHPFRC). Int J Fatigue 2024;180. https://doi.org/10.1016/j.ijfatigue.2023.108103.

[28] González DC, Mena-Alonso Á, Mínguez J, Martínez JA, Vicente MA. Effect of fiber orientation on the fatigue behavior of steel fiber-reinforced concrete specimens by performing wedge splitting tests and computed tomography scanning. Int J Concr Struct Mater 2024;18:4. https://doi.org/10.1186/s40069-023-00639-8.

[29] Vicente MA, Ruiz G, González DC, Mínguez J, Tarifa M, Zhang X. Effects of fiber orientation and content on the static and fatigue behavior of SFRC by using CT-Scan technology. Int J Fatigue 2019;128:105178. https://doi.org/10.1016/j.ijfatigue.2019.06.038.

[30] Meng S, Jiao C, Ouyang X, Niu Y, Fu J. Effect of steel fiber-volume fraction and distribution on flexural behavior of Ultra-high performance fiber reinforced concrete by digital image correlation technique. Constr Build Mater 2022;320. https://doi.org/10.1016/j.conbuildmat.2021.126281.

[31] Zhang S, Liao L, Song S, Zhang C. Experimental and analytical study of the fibre distribution in SFRC: A comparison between image processing and the inductive test. Compos Struct 2018;188:78–88. https://doi.org/10.1016/j.compstruct.2018.01.006.

[32] Cavalaro SHP, López-Carreño R, Torrents JM, Aguado A, Juan-García P. Assessment of fibre content and 3D profile in cylindrical SFRC specimens. Mater Struct/Mater Et Constr 2016;49:577–95. https://doi.org/10.1617/s11527-014-0521-2.

[33] Badran A, Marshall D, Legault Z, Makovetsky R, Provencher B, Piché N, et al. Automated segmentation of computed tomography images of fiber-reinforced composites by deep learning. J Mater Sci 2020;55:16273–89. https://doi.org/10.1007/s10853-020-05148-7.

[34] Tian W, Cheng X, Liu Q, Yu C, Gao F, Chi Y. Meso-structure segmentation of concrete CT image based on mask and regional convolution neural network. Mater Des 2021;208. https://doi.org/10.1016/j.matdes.2021.109919.

[35] Balázs GL, Czoboly O, Lublóy É, Kapitány K, Barsi Á. Observation of steel fibres in concrete with Computed Tomography. Constr Build Mater 2017;140:534–41. https://doi.org/10.1016/j.conbuildmat.2017.02.114.

[36] Skarżyński J, Suchorzewski. Mechanical and fracture properties of concrete reinforced with recycled and industrial steel fibers using Digital Image Correlation technique and X-ray micro computed tomography. Constr Build Mater 2018;183:283–99. https://doi.org/10.1016/j.conbuildmat.2018.06.182.

[37] Groeneveld AB, Ahlborn TM, Crane CK, Burchfield CA, Landis EN. Dynamic strength and ductility of ultra-high performance concrete with flow-induced fiber alignment. Int J Impact Eng 2018;111:37–45. https://doi.org/10.1016/j.ijimpeng.2017.08.009.

[38] Zhou B, Uchida Y. Influence of flowability, casting time and formwork geometry on fiber orientation and mechanical properties of UHPFRC. Cem Concr Res 2017;95:164–77. https://doi.org/10.1016/j.cemconres.2017.02.017.

[39] González DC, Mínguez J, Vicente MA, Cambronero F, Aragón G. Study of the effect of the fibers' orientation on the post-cracking behavior of steel fiber reinforced concrete from wedge-splitting tests and computed tomography scanning. Constr Build Mater 2018;192:110–22. https://doi.org/10.1016/j.conbuildmat.2018.10.104.

[40] Mínguez J, González DC, Vicente MA. Fiber geometrical parameters of fiber-reinforced high strength concrete and their influence on the residual post-peak flexural tensile strength. Constr Build Mater 2018;168:906–22. https://doi.org/10.1016/j.conbuildmat.2018.02.095.

[41] González DC, Mena Á, Mínguez J, Vicente MA. Influence of air-entraining agent and freeze-thaw action on pore structure in high-strength concrete by using CT-Scan technology. Cold Reg Sci Technol 2021;192:103397. https://doi.org/10.1016/j.coldregions.2021.103397.

[42] Kang SH, Hong SG, Moon J. The effect of superabsorbent polymer on various scale of pore structure in ultra-high performance concrete. Constr Build Mater 2018;172:29–40. https://doi.org/10.1016/j.conbuildmat.2018.03.193.

[43] Yang Z, Ren W, Sharma R, McDonald S, Mostafavi M, Vertyagina Y, et al. In-situ X-ray computed tomography characterisation of 3D fracture evolution and image-based numerical homogenisation of concrete. Cem Concr Compos 2017;75:74–83. https://doi.org/10.1016/j.cemconcomp.2016.10.001.

[44] Nitka M, Tejchman J. A three-dimensional meso-scale approach to concrete fracture based on combined DEM with X-ray μCT images. Cem Concr Res 2018;107:11–29. https://doi.org/10.1016/j.cemconres.2018.02.006.

[45] UNE-EN 12350–8. Testing fresh concrete. Part 8: Self-compacting concrete. Slump-flow test, 2011.

[46] EFNARC (The European Federation of Specialist Construction Chemicals and Concrete Systems), The European Guidelines for Self-Compacting Concrete. Specification, Production and Use, 2005.

[47] European Committee for Standardisation (CEN), UNE-EN 14651. Test method for metallic fibre concrete. Measuring the flexural tensile strength (limit of proportionality (LOP), residual), 2008.

[48] Grégoire D, Rojas-Solano LB, Pijaudier-Cabot G. Failure and size effect for notched and unnotched concrete beams. Int J Numer Anal Methods Geomech 2013;37:1434–52. https://doi.org/10.1002/nag.2180.

[49] Yang J, Chen B, Nuti C. Influence of steel fiber on compressive properties of ultra-high performance fiber-reinforced concrete. Constr Build Mater 2021;302. https://doi.org/10.1016/j.conbuildmat.2021.124104.

[50] Gesoglu M, Güneyisi E, Muhyaddin GF, Asaad DS. Strain hardening ultra-high performance fiber reinforced cementitious composites: effect of fiber type and concentration. Compos B Eng 2016;103:74–83. https://doi.org/10.1016/j.compositesb.2016.08.004.
[51] Banjara NK, Ramanjaneyulu K. Experimental investigations and numerical simulations on the flexural fatigue behavior of plain and fiber-reinforced concrete. J Mater Civ Eng 2018;30:1–15. https://doi.org/10.1061/(ASCE)MT.1943-5533.0002351.
[52] Carlesso DM, de la Fuente A, Cavalaro SHP. Fatigue of cracked high performance fiber reinforced concrete subjected to bending. Constr Build Mater 2019;220:444–55. https://doi.org/10.1016/j.conbuildmat.2019.06.038.
[53] Ríos JD, Cifuentes H, Blasón S, López-Aenlle M, Martínez-De La Concha A. Flexural fatigue behaviour of a heated ultra-high-performance fibre-reinforced concrete. Constr Build Mater 2021;276:122209. https://doi.org/10.1016/j.conbuildmat.2020.122209.
[54] González DC, Moradillo R, Mínguez J, Martínez JA, Vicente MA. Postcracking residual strengths of fiber-reinforced high-performance concrete after cyclic loading. Struct Concr 2018;19:340–51. https://doi.org/10.1002/suco.201600102.
[55] Laranjeira F, Grünewald S, Walraven J, Blom C, Molins C, Aguado A. Characterization of the orientation profile of steel fiber reinforced concrete. Mater Struct/Mater Et Constr 2011;44:1093–111. https://doi.org/10.1617/s11527-010-9686-5.
[56] Lorente S, Carmona S, Molins C. Use of fiber orientation factor to determine residual strength of steel fiber reinforced concrete. Constr Build Mater 2022;360. https://doi.org/10.1016/j.conbuildmat.2022.128878.